Materials Science and Engineering B 177 (2012) 303–310

Contents lists available at SciVerse ScienceDirect

Materials Science and Engineering B

journal homepage: www.elsevier.com/locate/mseb

Vibration frequency of graphene based composites: A multiscale approach

Y. Chandra [a], R. Chowdhury [b,*], F. Scarpa [c], S. Adhikari [b], J. Sienz [a], C. Arnold [d], T. Murmu [d], D. Bould [a]

[a] ASTUTE Project, Swansea University, Swansea SA2 8PP, UK
[b] Multidisciplinary Nanotechnology Center, Swansea University, Swansea SA2 8PP, UK
[c] Advanced Composites Centre for Innovation and Science, University of Bristol, Bristol BS8 1TR, UK
[d] Welsh Composite Center, Swansea University, Swansea SA2 8PP, UK

ARTICLE INFO

Article history:
Received 9 July 2011
Received in revised form 31 October 2011
Accepted 5 December 2011
Available online 20 December 2011

Keywords:
Graphene sheets
Composites
Atomistic model
Natural frequencies

ABSTRACT

This paper presents a multiscale approach for vibration frequency analysis of graphene/polymer composites. The graphene is modelled at the atomistic scale, and the matrix deformation is analysed by the continuum finite element method. Inter-connectivity between graphene and polymer matrix are assumed to be bonded by van der Waals interactions at the interface. The impact of geometrical configuration (armchair and zigzag), boundary conditions and length on the overall stiffness of the graphene reinforced plastics (GRP) is studied. The natural frequency and vibrational mode shapes of GRP studied have displayed dependence on the length and also the boundary conditions. The exceptional vibrational behaviour and large stiffness displayed by GRP makes them a potential replacement for conventional composite fibres such as carbon and glass fibres.

1. Introduction

Graphene [1] consists of an array of carbon atoms arranged hexagonally and the atoms are paired by strong covalent sp^2 bonds. The length of sp^2 covalent bond is 0.142 nm. The cylindrical formation of such sheet will form carbon nanotube (CNT) [2]. A spherical enclosure of the graphene sheet results in buckyballs [3,4]. These nano materials are the strongest and stiffest materials discovered till date. The exceptional mechanical properties of such nanostructures have already been demonstrated by several researchers [5–11]. These properties as well as their high aspect ratio (AR) and low density suggest that graphene may hold promise as the reinforcement for nanocomposites [12–14]. The improvement in stiffness and strength due to the addition of carbon nanostructures in polymeric matrix materials have been demonstrated [15,16]. For the effective utilization of graphene as reinforcements in composites, various attempts have been made [17,18]. Meanwhile, some efforts have also been devoted to the study of the load transfer between graphene/CNT and the matrix [12,19,20]. The transmission electron microscopy study of Rafiee et al. [12] indicated that unzipping CNT into graphene nanoribbons results in a significant improvement in load transfer effectiveness. On the other hand, the exceptional scale of electrical conductivity [21,22] displayed by these thin carbon films embedded [23,24] in polymer matrix [25], will make them suitable candidate in aerospace applications that require protection from lightning strikes. Apart from structural applications, graphene based composites [26,27,16,28,29] are expected to play a prominent role in various other domains including electrical devices, biosensors [30,31], fuel cells and packaging [70].

Due to the difficulty in modelling nano-composites, studies on the mechanisms of load transfer [32] between the matrix and CNT/graphene are very limited [33,34]. Among the available literature, Li and Chou [35] used molecular structural mechanics to study the compressive behaviour of CNT-polymer composites. As per the review conducted by Hussain et al. [25], there is a growing market demand for nano composites and also the authors pointed out at various issues such as inability to attain strong bonding between matrix and fibre, difficulty in dispersion of nanoparticles in matrix and alignment issues. Manufacturing techniques for graphene based composites has been discussed by many authors [16,28,29].

With regard to the structural analysis of graphene two distinct types of methods, namely atomistic finite element method [36–43] and continuum finite element method [37,44,45] have been proposed in literature. More recently non-local continuum methods [46,47] have been proposed in order to capture small-scale effects within the scope of the continuum theory. The authors have recently developed a numerical model of graphene sheets, in which equivalent homogenized properties are expressed in terms of the thickness, equilibrium lengths and force-field models [2,48] used to represent the C—C bonds of the graphene lattice [10,8]. The covalent bonds between pair of carbon atoms are modelled

* Corresponding author. Tel.: +44 01792 602088; fax: +44 01792 295676.
E-mail addresses: R.Chowdhury@Swansea.ac.uk, crajib2003@gmail.com (R. Chowdhury).

0921-5107/$ – see front matter © 2011 Elsevier B.V. All rights reserved.
doi:10.1016/j.mseb.2011.12.024

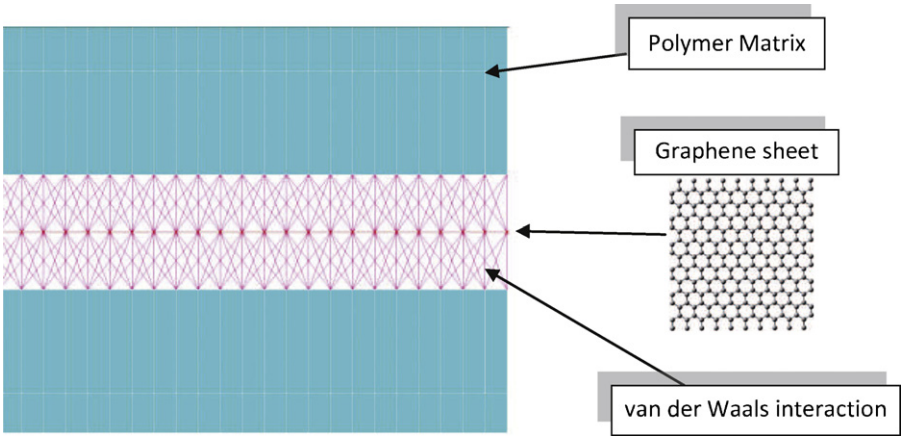

Fig. 1. Multiscale model of GRP: Carbon atoms are represented by nodes, covalent bonds are modelled by Timoshenko beams, L–J potential is modelled by spring elements and the polymer matrix is formed by 3D solid elements. The tool used is ANSYS 13 [69].

by deep shear Timoshenko beams [49] with stretching, bending, torsional and deep shear deformation. The properties of these deep shear beams are derived based on the equivalence between the harmonic potential. The force constants of this harmonic potential can be either based on Morse model or Amber model (see for example [50,8]). The geometric configurations and mechanical properties are represented as truss assemblies (finite elements) are then calculated minimizing the total potential energy associated to the loading, thickness and average equilibrium lengths of the bonds. The polymer matrix is represented by 3D continuum elements. These continuum elements offer three translation and three rotational degrees of freedom to the polymer structure. The weak bonding between the matrix and the fibre is modelled with the aid of Lennard–Jones (L–J) potential theory, where bonds are represented by springs. This approach can be termed as multiscale modelling procedure, since the graphene sheet is represented at atomic scale and the polymer matrix is represented by continuum elements (i.e. macro scale). The finite element model of the GRP is depicted in Fig. 1. The impact of different geometrical configurations (armchair and zigzag), boundary conditions and AR on the GRP are studied in the present study. In this paper, we examine the dynamical behaviour of graphene–polymer composites using a multiscale modelling approach. We propose also an analytical plate model to simulate in a compact form the mechanical vibrational behaviour of GRP, providing a further benchmark to the multiscale finite element (FE) model of the GRP.

2. Continuum model of GRP

At larger dimensions, a GRP sheet may be represented by an elastic plate with an equivalent thickness. The governing equation of motion of such an elastic plate subjected to flexural vibrations is given by [49,51–53]:

$$D\left(\frac{\partial^4 w}{\partial x^4}+2\frac{\partial^2 w}{\partial x^2}\frac{\partial^2 w}{\partial y^2}+\frac{\partial^4 w}{\partial y^4}\right)+\rho\frac{\partial^2 w}{\partial t^2}=0 \tag{1}$$

where $w \equiv w(x, y, t)$ is the displacement vector at x, y coordinates of the plate, t is the time, ρ is the mass density. The bending rigidity D [49] is given by

$$D=\frac{E(h+2d)^3}{12(1-\nu^2)} \tag{2}$$

where E is Young's modulus, h is the interlayer distance, d is the total thickness of GRP, and ν is the Poisson's ratio of the equivalent GRP. The natural frequency of such a structure with dimensions $a \times b$ is given by [54]

$$\omega_{ij}=\left\{\frac{\pi^4 D}{a^4\rho}\right\}^{1/2}\left\{G_x^4+G_y^4\left(\frac{a}{b}\right)^4+2\left(\frac{a}{b}\right)^2[\nu H_x H_y+(1-\nu)J_x J_y]\right\}^{1/2} \tag{3}$$

where $i, j = 1, 2, 3, \ldots$ are mode indices. The values of the coefficients G_x, H_x, J_x and G_y, H_y, J_y for three different boundary conditions are given in Table 1.

In the GRP composite structure, the matrix is bonded with the graphene fibre by L–J potential force. This is similar to the L–J potential sandwich found between pair of single-layer graphene sheets (SLGS) in the case of multi-layer graphene sheets [10]. The equivalent Young's modulus E_{eq} and the density ρ_{eq} of the GRP can be determined with the aid of standard rule of mixture for unidirectional composites [55], and neglecting the stiffness contribution of the L–J potential:

$$E_{eq}=(E_{Graphene}V_{Graphene})+(E_{Matrix}V_{Matrix}) \tag{4}$$

$$\rho_{eq}=(\rho_{Graphene}V_{Graphene})+(\rho_{Matrix}V_{Matrix}) \tag{5}$$

The Young's modulus and density calculated by the above equation has been considered for the calculation of elastic plate natural frequencies using Eq. (3).

3. Multiscale finite element approach for the GRP

The need for a multiscale approach arises from the fact that the length-scale of graphene is significantly different from that of the surrounding polymer. Majority of existing multiscale approach [56] aims to combine Molecular Dynamic (MD) simulation with finite element method. MD method is used for the nano scale, while FE method is for the macro scale. In this paper we are proposing a new approach where atomistic finite element method is used in the nano scale and continuum finite element method is used for the macro scale. The main advantage of the proposed method is that both type of finite element method can be integrated in a consistent manner.

3.1. Modelling of sp^2 bonds: atomistic finite element method

A graphene sheet consists of hexagonal array of covalently bonded carbon atoms. The details of the atomistic finite element can be found in [8,57]. Here we give a brief overview of the method. The sp^2 covalent bonds between the pair of carbon atoms can be modelled by Timoshenko beams having axial, out-of-plane

Table 1
Coefficients for the various boundary conditions.

BC	i	j	G_x	H_x	J_x	G_y	H_y	J_y
Cantilever (CFFF)	1	0	0.597	−0.087	0.471	0.0	0.0	0.0
Bridged (CCFF)	1	0	1.506	1.248	1.248	0.0	0.0	0.0
Simply supported	1	0	1	1	1	1	1	1

and in-plane rotational deformation mechanisms. These bonds are influenced by harmonic potential [58] and is given by:

$$U_r = \frac{1}{2}k_r(\delta r)^2, \qquad U_\theta = \frac{1}{2}k_\theta(\delta\theta)^2 \quad \text{and} \quad U_\tau = \frac{1}{2}k_\tau(\delta\varphi)^2 \tag{6}$$

Here U_r, U_θ and U_τ are respectively the energies due to bond stretching, bond angle variation, and combined dihedral angle and out-of-plane torsion. k_r, k_θ and k_τ are respectively the force constants related to bond stretching, bending and torsional stiffness. The equivalent mechanical properties of the covalent bond can be determined using a beam mapping procedure, imposing the equivalence between the harmonic potential and the mechanical strain energies of a hypothetical structural beam of length L [50]:

$$\frac{k_r}{2}(\delta r)^2 = \frac{EA}{2L}(\delta r)^2, \tag{7}$$

$$\frac{k_\tau}{2}(\delta\varphi)^2 = \frac{GJ}{2L}(\delta\varphi)^2 \quad \text{and} \tag{8}$$

$$\frac{k_\theta}{2}(\delta\theta)^2 = \frac{EI}{2L}\frac{4+\Phi}{1+\Phi}(\delta\theta)^2 \tag{9}$$

Eq. 7 accounts for stretching and axial deformation mechanism (where E is the Young's modulus), while Eq. (8) represents the torsional deformation mechanism (where G is shear modulus). The in-plane rotation term of the C—C bond (Eq. (9)) is equated to a bending strain energy related to a deep shear beam model, in order to consider the shear deformation of the cross section. The shear correction factor is essential if AR of beams is lower than 10 [49]. The shear deformation constant for beams with the circular cross sections considered is given by [50]:

$$\Phi = \frac{12EI}{GA_sL^2} \tag{10}$$

In Eq. (10), $A_s = A/F_s$ is the reduced cross section of the beam by the shear correction term F_s [59]:

$$F_s = \frac{6+12\nu+6\nu^2}{7+12\nu+4\nu^2} \tag{11}$$

Equating Eqs. (10) and (11) in (2) results in an nonlinear relation between the beam thickness d and the beam Poisson's ratio ν [50]:

$$k_\theta = \frac{k_r d^2}{16}\frac{4A+B}{A+B} \tag{12}$$

where:

$$A = 112L^2k_\tau + 192L^2k_\tau\nu + 64L^2k_\tau\nu^2 \tag{13}$$

$$B = 9k_rd^2 + 18k_rd^4\nu + 9k_rd^4\nu^2 \tag{14}$$

As per the Morse model [8], the magnitude of force constants are $k_r = 8.74\times10^{-7}$ N nm^{-1}, $k_\theta = 9.00\times10^{-10}$ N nm rad^{-2} and $k_\tau = 2.78\times10^{-10}$ N nm^{-1} rad^{-2}. The mechanical properties of the covalent bond can be calculated by a nonlinear optimization of Eqs. (7)–(9) using a Marquardt algorithm [60]. In the context of finite elements, the C—C bond can then be modelled as a two-nodded three dimensional beam with a stiffness matrix presented in [61]. In this methodology the nodes represent the carbon atoms. This atomistic model of graphene fibres consisting of beams representing covalent bonds and nodes representing carbon atoms can be seen in Fig. 1. In this numerical procedure, at each substep of the Newton–Raphson solver technique [62] the total potential energy is minimized, to determine the thickness of the C—C bonds and the average equilibrium length of the covalent bonds. The nonlinear minimization technique is performed in two steps, with a zero order method to identify first the minimal clusters, and a subsequent first order derivative-based method to identify the absolute minimum of the potential energy. The details about this atomistic modelling technique can be found in [57].

Within the finite element model of fibre, the mass and stiffness matrices are generated from the equivalent matrices of the beams representing C—C bonds and concentrated masses of carbon atom at each node. The diagonal lumped mass matrix for a single beam element is given by:

$$[\mathbf{M}]_\mathbf{e} = diag\left[\frac{m_c}{3} \quad \frac{m_c}{3} \quad \frac{m_c}{3} \quad 0 \quad 0 \quad 0\right] \tag{15}$$

where $m_c = 1.9943\times10^{-26}$ kg is the mass of a carbon atom. The general equation of motion of the undamped system ($[\mathrm{K}]\mathrm{x} + [\mathrm{M}]\ddot{\mathbf{x}} = 0$) leads to a standard undamped eigenvalue problem ($([\mathbf{K}] - \omega^2[\mathbf{M}])\{\mathbf{x}\} = \{\mathbf{0}\}$), which has been solved using a Block Lanczos algorithm [63].

3.2. Modelling the polymer matrix: continuum finite element method

The modelling approach employed here is similar to the one adopted for simulating CNT polymer composite by the researchers [23]. modelling of continuous molecular chain of polymer is computationally expensive. Because of this computational issue, the polymer matrix at micro scale can be approximated by a continuous structure. This continuous structure has been numerically discretized using 3D solid finite elements with six degrees of freedom (i.e. translations and rotations in x, y, z coordinates). The material properties are assumed to be isotropic with Young's modulus 4 GPa and Poisson's ratio 0.3. These solid elements are connected to the graphene fibre carbon atoms by L–J potential forces represented by springs. The modelling procedure of these L–J potential forces will be discussed in the next section. The depth of the polymer matrix on both sides of the SLGS has been chosen to represent 95% volume fraction. The FE representation of the polymer matrix can be seen in Fig. 1.

3.3. Modelling the fibre-matrix potential

The modelling approach employed here is similar to the one adopted for simulating L–J potential springs between two layers of graphene sheets in the case of bi-layer graphene sheet (BLGS) [8]. The equivalent axial force related to the L–J potential between pair of atoms (i, j) belonging to different graphene layer and the matrix is expressed as:

$$F_{ij} = \frac{\partial V_{ij}}{\partial r} \tag{16}$$

where, r is the atomic displacement along **ij** (fibre-matrix length). According to Girifalco et al. [3], the force between the atoms (ij) can also be represented by

$$F_{ij} = -12\epsilon\left[\left(\frac{r_{min}}{y}\right)^{13} - \left(\frac{r_{min}}{y}\right)^{7}\right] \tag{17}$$

where, $y = r_{min} + \delta r$, δr is the atomic displacement along the length **ij**. The r_{min} (in Å) is given by $2^{1/6}\,\sigma$, where $\sigma = (A/B)^{1/6}$. The B and A are attractive and repulsive constants, and for the boundary conditions considered in this paper, they are given by 3.4×10^{-4} eV Å^{12} and 5×10^{-7} eV Å^{6} respectively, and ϵ is $B^2/(4A)$. These constants have been calculated based upon the van der Waals forces between graphene and polymer matrix [23]. In the multiscale models, we have used spring elements to form a nonlinear connection between fibre and matrix representing L–J potentials. The L–J potential springs require force deflection curve as a property and has been calculated by using Eq. (17).

The method used in this paper to describe the mechanical behaviour of the graphene-based nanocomposite is based on a hybrid FE approach. While the matrix is simulated using 3D solid elements with a continuum homogenized isotropic material, the graphene sheet is represented by a lattice assembly of C—C sp^3 bonds through 3D Timoshenko beam [50,65] elements. Springs representing the nonlinear force–displacement behaviour corresponding to L–J potentials [50,57] simulate the interaction between the graphene and the mesoscale-surrounding matrix. The novelty of this approach compared to analogous matrix/graphene representations in open literature [64] is the lattice representation of the graphene-L–J potentials. More specifically, the C—C bonds in the graphene sheet are represented using deep-shear Timoshenko beam elements. Their equivalent mechanical properties are obtained through a nonlinear minimization of the equivalence between the stoichiometric harmonic potentials associated to stretching, in-plane bending and out-of-plane torsion of the bonds, and the equivalent strain energies associated to deep shear Timoshenko beams. The use of Timoshenko beams allows to overcome an lack of congruence existing when Euler–Bernoulli beams [36,58] are employed – i.e., the identification of a thickness almost equal to the equilibrium length [58], and therefore a slenderness ratio close to 1, which is in contrast with the assumption of bending beam theory [49]. The value of the equivalent C—C bond thickness identified assuming a transversely isotropic equivalent material for the bond is dependent on the force model used and the type of loading applied to the nanostructure [50,65]. Moreover, when an equivalent full isotropic material and circular cross-section for the C—C bond beam is assumed, the values of the thickness are unique and close to the values identified for graphene structures through Molecular Dynamics methods [5,66].The determination in a rigorous mechanics of solids manner of the C—C bond thickness allow to avoid the so-called 'Yakobson's paradox' [67], and not to adopt the classical value of 0.34 nm, which corresponds to the interlayer distance of graphite, but it is not the thickness of a continuum graphene sheet per se. The L–J-based springs used to represent the interaction between the SLGS and the matrix are calculated based on the equilibrium conditions at the graphitic state between the graphene and the surrounding polymer matrix. The distribution of neighbour and near-neighbour interactions between atoms of the graphene and atoms of the matrix (represented by the nodes of the continuum elements) provides a more detailed and discrete simulation of the mechanical deformation between the SLGS the matrix at mesoscale level, avoiding the use of an equivalent normal pressure distribution for the L–J interaction as in [64]. The present hybrid FE model shown in this work is therefore a more detailed representation at nano-mesoscale level of a graphene sheet in graphitic equilibrium state embedded into a polymeric matrix.

3.4. Boundary conditions

At nano scale, the atomic configurations influence the mechanical properties of graphene sheets and in turn govern the behaviour of GRP. The zigzag and armchair fibre configurations are modelled in this article. The boundary conditions considered on the zigzag and armchair models of the graphene fibre are:

- GRP1: Armchair model clamped at one edge (Cantilevered condition)
- GRP2: Armchair model clamped at two opposite edges (Bridged condition)
- GRP3: Zigzag model clamped at one edge (Cantilevered condition)
- GRP4: Zigzag model clamped at two opposite edges (Bridged condition)

Pictorial representation of the four GRP models are shown in Fig. 2.

4. Results and discussion

The geometric configurations play a vital role in deciding the performance of GRP based devices. Due to this, we study two different configurations namely zigzag and armchair with varying length and width. A preliminary dynamic analysis on the unconstrained model has been performed in order to ensure the integrity of the GRP structure. The first four mode shapes for the cases GRP1 and GRP2 are presented in Figs. 3 and 4, respectively. The AR of these models is 5 and the width is 1.49 nm. In the case of the cantilevered model, the first and fourth mode shapes are flexural in nature, second mode is found to be torsional and the third mode shape is in plane bending type. For the case of the bridged model, the first, second and fourth mode shapes are flexural, and the third mode shape is found to be out of plane twisting.

4.1. Dependence on the length and AR

The fundamental frequency results of armchair and zigzag GRP are shown in Fig. 5, for bridged and cantilevered boundary conditions. As per these figures, with increasing length from about 1.5 nm to about 16 nm of the cantilever armchair GRP (width = 4.33 nm), the range of first natural frequencies is found to be 156–5 GHz. Whereas for the zigzag model, this range is found to be 104–5 GHz. For the bridge boundary condition case, the armchair GRP exhibits the range 242–22 GHz and the zigzag model exhibits the range 184–20 GHz. This pattern of variation is found to be similar in the cases of single layer graphene sheets SLGS [5,6] and also BLGS [57]. These observations indicate that GRP offers natural frequency half of that of SLGS [5,6] and 1/6th of that of BLGS [57]. Similar to BLGS, the percentage decreases of the natural frequency with length are based upon the series of increasing powers (ar^j, where $j = 0, 1, 2, \ldots$). In this series a is a scale factor, which can be considered as the natural frequency associated to the lowest considered length and r is a common ratio which lies between a range of 0.6–0.5 approximately.

The dependence of natural frequencies on length at a given AR is given in Fig. 6. These patterns of variation of frequencies are similar to those obtained for BLGS [57] and SLGS [5,6]. This indicates that the such pattern of variation for GRP nanocomposites is similar to that of nano structures SLGS and BLGS. As per Fig. 6, the value of the natural frequency at length 1.78 nm and AR 0.2 is identical with the natural frequency of length 1.78 nm and AR = 0.4, i.e., at width reduction of about 50%.

4.2. Dependence on the boundary condition

As per the classical vibration theory of plates [53], a cantilever structure is found to be weaker than the bridge structure. According to Fig. 5, the alteration of boundary condition from one edge constrained to two edges constrained will enhance the natural frequency by a factor of 1.5. The trend is found to be same for second

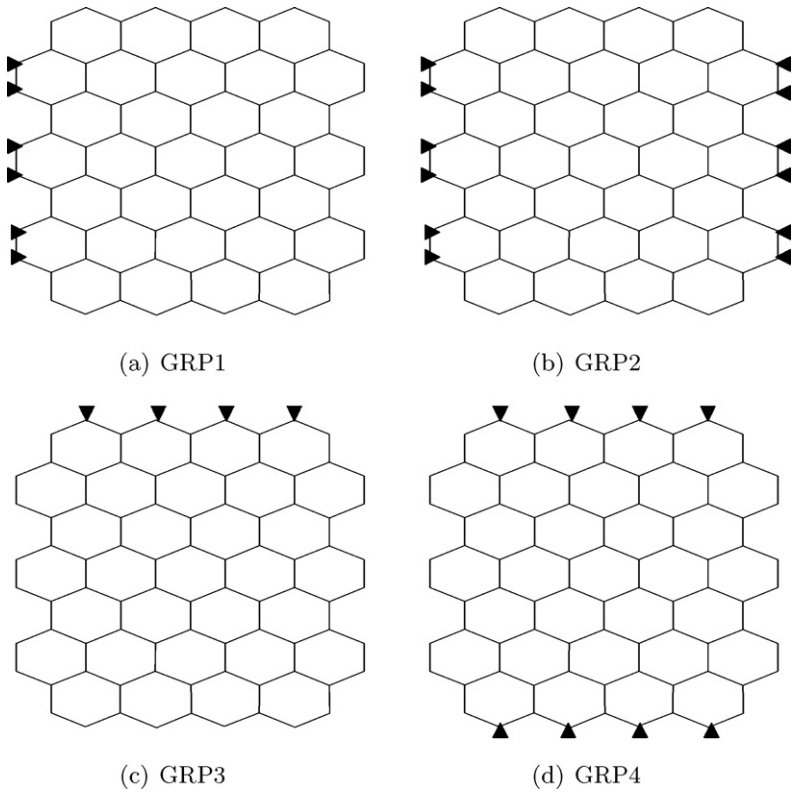

Fig. 2. Four GRP models: GRP1 = Armchair cantilevered, GRP2 = Armchair bridged, GRP3 = Zigzag cantilevered, GRP4 = Zigzag bridged.

fundamental frequency. Constraining this GRP structure at all edges will further stiffen the structure and in turn increase the natural frequency. It can also be noted that, with the increase in AR, the rate at which the natural frequency decreases with length is found to be higher for cantilever GRP as compared to the bridge GRP. According to these findings, it can be noted that GRP2 and GRP4 configurations are appropriate for nano-electro-mechanical devices, where higher fundamental frequencies are essential [31,68], whereas GRP1 and GRP3 are appropriate for low resonant frequency applications.

4.3. The influence of chirality

From the changing trends of the curves in Fig. 5, it is obvious that the influence of chirality on the natural frequency is very small. For identical lengths, the frequencies of armchair GRP are slightly higher than that of zigzag GRP for bridged case. But, this influence of atomic configuration on natural frequency becomes negligible at higher lengths. The maximum relative difference calculated by the relation $(\omega_{armchair} - \omega_{zigzag})/\omega_{armchair}$ is found to be about 0.23 and

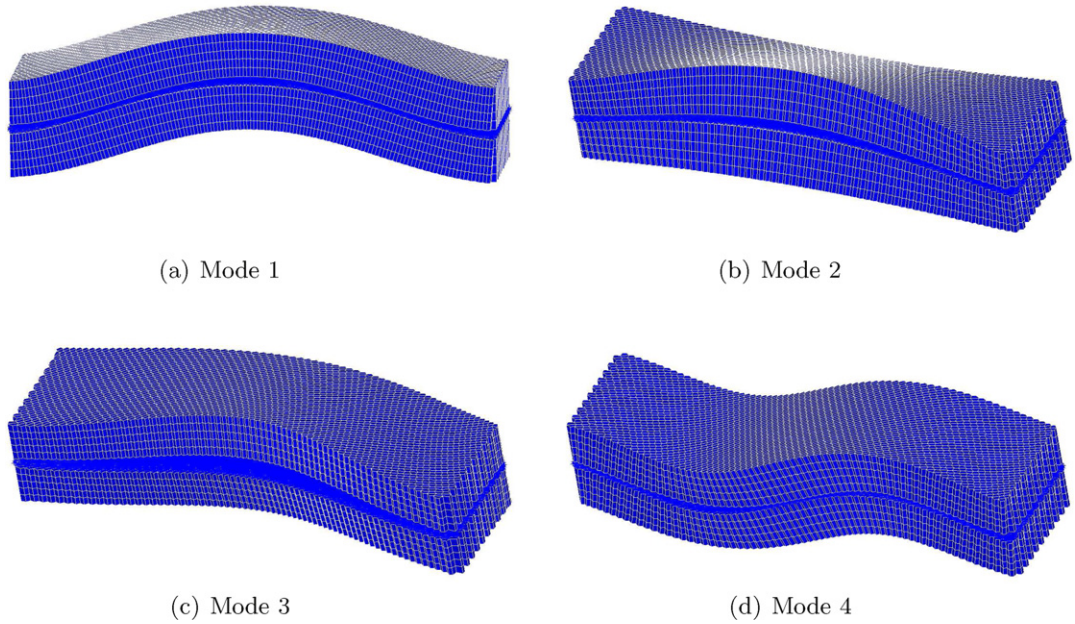

Fig. 3. The first four mode shapes of GRP1 with AR 5 and width 1.49 nm: (a) Mode 1 – bending; (b) Mode 2 – torsional; (c) Mode 3 – in plane bending; (d) Mode 4 – bending.

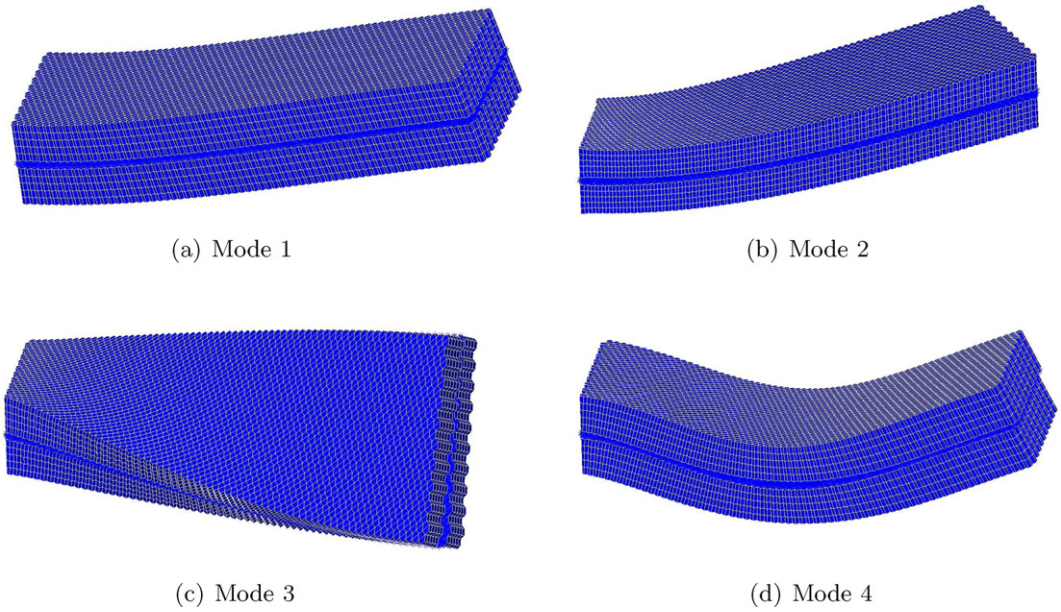

Fig. 4. The first four mode shapes of GRP2 with AR 5 and width 1.49 nm: (a) Mode 1 – bending; (b) Mode 2 – bending; (c) Mode 3 – out of plane twisting; (d) Mode 4 – bending.

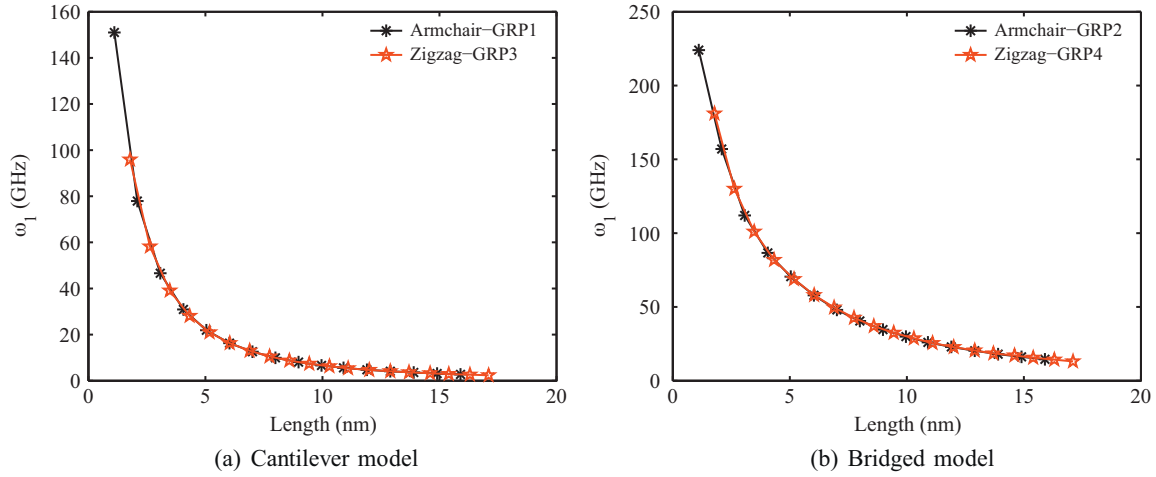

Fig. 5. The variation of the fundamental frequency with length: (a) Cantilevered boundary condition – fundamental frequencies of armchair and zigzag GRP as a function of the length. Selected widths are – GRP1: 4.33 nm and GRP3: 4.06 nm; (b) Bridged boundary condition – fundamental frequencies of armchair and zigzag GRP as a function of the length. The widths are – GRP2: 4.33 nm; GRP4: 4.06 nm.

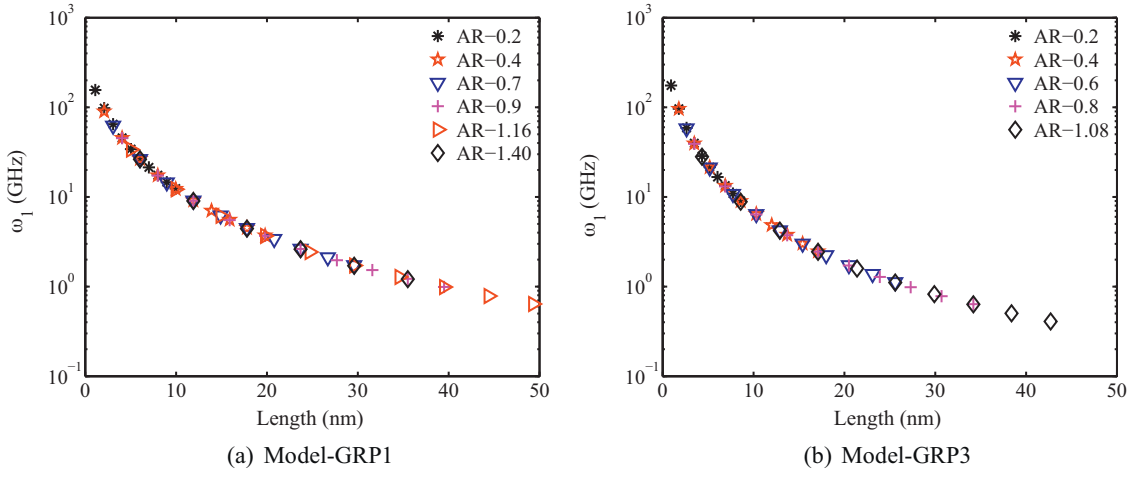

Fig. 6. The variation of natural frequencies with length at a given AR.

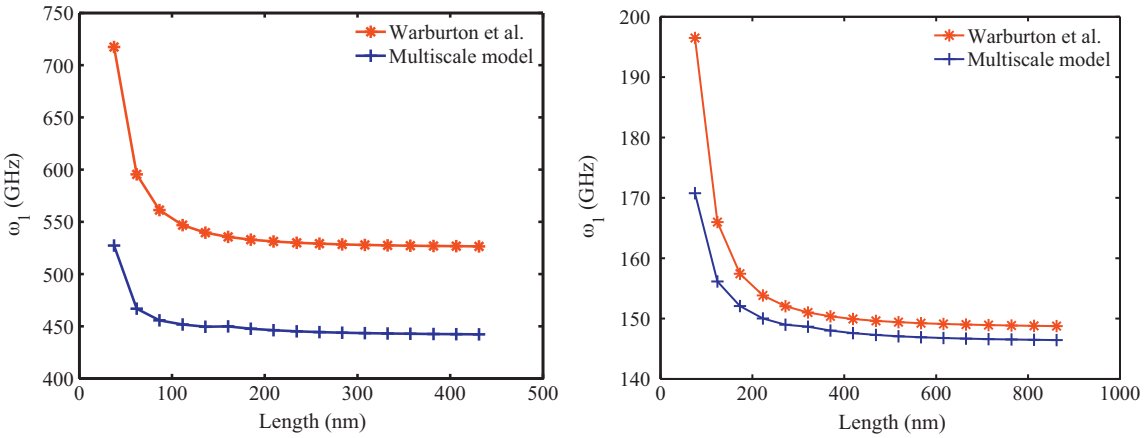

(a) GRP of lower dimensions (width = 22.80 nm) (b) GRP of larger dimensions (width = 42.80 nm)

Fig. 7. Boundary condition is simply supported at all edges – vibrational resonant frequencies of the GRP. Numerically computed frequencies are compared against those of analytical computed at varying length. Significant error margin (∼28%) has been identified for lower sized models (width = 22.80 nm). But the models of larger dimensions (width = 42.8 nm) display negligible error. At larger lengths (above 400 nm), very lower error margin (∼5%) has been identified.

0.33 for bridge and cantilever models, respectively. These relative difference values are found to be 0.31 and 0.35 for the case of BLGS [57]. Whereas for the case of CNT this relative difference value is found to be as low as 0.08 [2]. These observations indicate that the influence of chirality is found to be identical for the cases of GRP and BLGS. Whereas this influence is found to be completely different, if a comparison is made between GRP and CNT.

4.4. Comparison with the continuum theory

The natural frequencies computed using Eq. (3) are compared against those from the multiscale-FE models, and presented in Fig. 7. The boundary condition considered in these cases is the simple supported at all edges. This boundary condition has been chosen since many terms of Eq 3 will vanish because of the values of coefficients (ref. Table 1). The low-dimensional models have been considered in Fig. 7(a). From this plot, a large difference can be observed between multiscale model and analytical model. The error margin found for these lower dimension models is as high as ∼28%. This large error occurs, since the lattice multiscale model will not form a close approximation of an elastic plate. Whereas for the GRP with larger dimension (Fig. 7(b)), the multiscale lattice model provides a closer approximation to the continuous elastic plate. At larger dimensions (lengths above 40 nm), the numerically computed frequencies are found to be very close to those calculated by continuum theory. The error margin is found to be as low as ∼5%. This observation confirms the fact that, a larger dimension model can be analysed by equivalent continuum elastic plate models. According to Table 2, it can be concluded that GRP modelled with the aid of continuum plate theory [53] displays higher values of the natural frequencies as compared to those of numerical multiscale model.

Table 2
Correlation of multiscale model results against continuum model results.

Length (nm)	ω [53] (GHz)	$\omega_{MultiscaleFE}$ (GHz)
75.0	196.5	168.2
124.0	166.0	154.1
173.0	157.0	151.07
223.0	154.0	148.01
272.0	152.0	144.97
321.0	151.0	142.02
370.0	150.4	141.21
419.0	150.0	140.22
469.0	149.6	139.42
518.0	149.4	139.25
567.0	149.2	137.02
616.0	149.1	136.14
665.0	149.0	135.13
714.0	148.9	133.18
764.0	148.8	132.38
813.0	148.7	130.20
862.0	148.5	129.34

Width of the GRP is 42.8 nm.

5. Conclusions

A multiscale finite element method has been proposed to study the natural frequencies and mode shapes of GRP composite structures. In the computational model the graphene fibre has been represented by truss type structure at the nano scale and the polymer matrix has been modelled using 3D hexahedral solid elements. The C—C bonds have been modelled by Timoshenko beams with stretching, bending, torsional and deep shear deformation capabilities. The properties of these beams have been calculated with the aid of Morse force-field model. The novelty of the proposed multiscale method is that it uses finite element approach at both scales – namely an atomistic finite element for the graphene and the conventional continuum finite element method for the surrounding polymer. This significantly reduces problems in interfacing the two scales, which often arises in the multiscale methods involving molecular dynamics and the finite element method.

The vibrational characteristics of GRP have been calculated by considering two types of graphene fibre configurations, namely zigzag and armchair. The modal behaviour of the composite GRP structure is found to be similar to that of displayed by SLGS and BLGS. Also pattern of variation of natural frequency of GRP with length, width and AR is found to be identical with that of BLGS and SLGS. Similar to the behaviour observed in SLGS and BLGS, the fundamental natural frequency of the GRP decreases with increasing length and AR. The natural frequency of the GRP at a given length is found to be lesser than that of SLGS and BLGS. This is due to the fact that stiffness of the GRP is influenced by the modulus of the polymer matrix rather than the graphene fibre (5% volume fraction). The bridged GRP is found to be offering higher natural frequencies as compared to cantilever GRP. This means bridge GRP is appropriate for high resonance applications. For smaller dimension GRP structure, the chirality influences the natural frequency. Whereas

the larger dimension GRP structures are found to be independent of chirality.

Acknowledgements

YC acknowledges the support given by the Welsh Assembly Government through the ASTUTE project. SA gratefully acknowledges the support of The Leverhulme Trust for the award of the Philip Leverhulme Prize.

References

[1] Y. Gan, W. Chu, L. Qiao, Surface Science 539 (1–3) (2003) 120–128.
[2] R. Chowdhury, S. Adhikari, C.Y. Wang, F. Scarpa, Computational Materials Science 48 (4) (2010) 730–735.
[3] L.A. Girifalco, M. Hodak, R.S. Lee, Physical Review B 62 (19) (2000) 13104–13110.
[4] S. Adhikari, R. Chowdhury, Physics Letters A 375 (22) (2011) 1276–1280.
[5] S.S. Gupta, R.C. Batra, Journal of Computational and Theoretical Nanoscience 7 (10) (2010) 2151–2164.
[6] R. Chowdhury, S. Adhikari, F. Scarpa, M.I. Friswell, Journal of Physics D: Applied Physics 44 (20) (2011), 205401:1–11.
[7] M.M. Shokrieh, R. Rafiee, Materials and Design 31 (2) (2010) 790–795.
[8] F. Scarpa, S. Adhikari, A. Phani, Nanotechnology 20 (6) (2009), 065709:1–11.
[9] M. Sadeghi, R. Naghdabadi, Nanotechnology 21 (10) (2010), 105705:1–10.
[10] F. Scarpa, R. Chowdhury, S. Adhikari, Physics Letters A 375 (20) (2011) 2071–2074.
[11] R. Chowdhury, C.Y. Wang, S. Adhikari, Journal of Physics D: Applied Physics 43 (085405) (2010) 1–8.
[12] M.A. Rafiee, W. Lu, A.V. Thomas, A. Zandiatashbar, J. Rafiee, J.M. Tour, N.A. Koratkar, ACS Nano 4 (12) (2010) 7415–7420.
[13] L.S. Walker, V.R. Marotto, M.A. Rafiee, N. Koratkar, E.L. Corral, ACS Nano 5 (4) (2011) 3182–3190.
[14] P. Mukhopadhyay, R.K. Gupta, Plastics Engineering 67 (1) (2011) 32–42.
[15] E.T. Thostenson, T.W. Chou, Journal of Physics D: Applied Physics 36 (5) (2003) 573–582.
[16] S. Stankovich, D.A. Dikin, G.H.B. Dommett, K.M. Kohlhaas, E.J. Zimney, E.A. Stach, R.D. Piner, S.T. Nguyen, R.S. Ruoff, Nature 442 (7100) (2006) 282–286.
[17] T. Ramanathan, A.A. Abdala, S. Stankovich, D.A. Dikin, M. Herrera-Alonso, R.D. Piner, D.H. Adamson, H.C. Schniepp, X. Chen, R.S. Ruoff, S.T. Nguyen, I.A. Aksay, R.K. Prud'homme, L.C. Brinson, Nature Nanotechnology 3 (6) (2008) 327–331.
[18] M.A. Rafiee, J. Rafiee, I. Srivastava, Z. Wang, H. Song, Z.-Z. Yu, N. Koratkar, Small 6 (2) (2010) 179–183.
[19] M.A. Rafiee, J. Rafiee, Z.Z. Yu, N. Koratkar, Applied Physics Letters 95 (22) (2009), 223103:1–3.
[20] J.R. Potts, D.R. Dreyer, C.W. Bielawski, R.S. Ruoff, Polymer 52 (1) (2011) 5–25.
[21] H.-B. Zhang, W.-G. Zheng, Q. Yan, Y. Yang, J.-W. Wang, Z.-H. Lu, G.-Y. Ji, Z.-Z. Yu, Polymer 51 (5) (2010) 1191–1196.
[22] J. Liang, Y. Wang, Y. Huang, Y. Ma, Z. Liu, F. Cai, C. Zhang, H. Gao, Y. Chen, Carbon 47 (3) (2009) 922–925.
[23] M.M. Shokrieh, R. Rafiee, Composite Structures 92 (3) (2010) 647–652.
[24] K.I. Tserpes, P. Papanikos, G. Labeas, S.G. Pantelakis, Theoretical & Applied Fracture Mechanics 49 (1) (2008) 51–60.
[25] F. Hussain, M. Hojjati, M. Okamoto, R.E. Gorga, Journal of Composite Materials 40 (17) (2006) 1511–1575.
[26] J. Liang, Y. Xu, Y. Huang, L. Zhang, Y. Wang, Y. Ma, F. Li, T. Guo, Y. Chen, Journal of Physical Chemistry C 113 (22) (2009) 9921–9927.
[27] R. Verdejo, M.M. Bernal, L.J. Romasanta, M.A. Lopez-Manchado, Journal of Materials Chemistry 21 (10) (2011) 3301–3310.
[28] R. Wissert, P. Steurer, S. Schopp, R. Thomann, R. Muelhaupt, Macromolecular Materials and Engineering 295 (12) (2010) 1107–1115.
[29] A.S. Patole, S.P. Patole, H. Kang, J.-B. Yoo, T.-H. Kim, J.-H. Ahn, Journal of Colloid and Interface Science 350 (2) (2010) 530–537.
[30] R. Chowdhury, S. Adhikari, P. Rees, F. Scarpa, S.P. Wilks, Physical Review B 83 (4) (2011), 045401:1–8.
[31] S. Adhikari, R. Chowdhury, Journal of Applied Physics 107 (12) (2010), 124322:1–8.
[32] L. Gong, I.A. Kinloch, R.J. Young, I. Riaz, R. Jalil, K.S. Novoselov, Advanced Materials 22 (24) (2010) 2694–2697.
[33] M.M. Shokrieh, R. Rafiee, Mechanics of Composite Materials 46 (2) (2010) 155–172.
[34] J.M. Wernik, S.A. Meguid, Applied Mechanics Reviews 63 (5) (2010), 050801:1–40.
[35] C. Li, T.-W. Chou, Composites Science and Technology 66 (14) (2006) 2409–2414.
[36] S.K. Georgantzinos, G.I. Giannopoulos, D.E. Katsareas, P.A. Kakavas, N.K. Anifantis, Computational Materials Science 50 (7) (2011) 2057–2062.
[37] J.-L. Tsai, S.-H. Tzeng, Y.-J. Tzou, International Journal of Solids and Structures 47 (3–4) (2010) 503–509.
[38] A. Masud, R. Kannan, International Journal for Numerical Methods in Engineering 78 (7) (2009) 863–882.
[39] R. Gracie, T. Belytschko, International Journal for Numerical Methods in Engineering 78 (3) (2009) 354–378.
[40] P.A. Guidault, T. Belytschko, International Journal for Numerical Methods in Engineering 77 (11) (2009) 1566–1592.
[41] R. Khare, S.L. Mielke, G.C. Schatz, T. Belytschko, Computer Methods in Applied Mechanics and Engineering 197 (41–42) (2008) 3190–3202.
[42] S. Zhang, R. Khare, Q. Lu, T. Belytschko, International Journal for Numerical Methods in Engineering 70 (8) (2007) 913–933.
[43] P. Chung, R. Narnburu, International Journal of Solids and Structures 40 (10) (2003) 2563–2588.
[44] J. Ghanbari, R. Naghdabadi, CMC-Computers Materials & Continua 10 (1) (2009) 41–64.
[45] A. Hemmasizadeh, M. Mahzoon, E. Hadi, R. Khandan, Thin Solid Films 516 (21) (2008) 7636–7640.
[46] T. Murmu, S. Adhikari, Composites Part B: Engineering 42 (7) (2011) 1901–1911.
[47] C.W. Wang, T. Murmu, S. Adhikari, Applied Physics Letters 98 (15) (2011), 153101:1–3.
[48] R. Chowdhury, C.Y. Wang, S. Adhikari, F. Scarpa, Nanotechnology 20 (12) (2010), 365702:1–9.
[49] S. Timoshenko, Theory of Plates and Shells, McGraw-Hill, Inc, London, 1940.
[50] F. Scarpa, S. Adhikari, Journal of Physics D: Applied Physics 41 (8) (2008), 085306:1–5.
[51] D.J. Gordman, Free Vibration Analysis of Rectangular Plates, Elsevier, New York, 1982.
[52] W. Soedel, Vibrations of Shells and Plates, 3rd ed., Marcel Dekker Inc., New York, 2004.
[53] G.B. Warburton, Proceedings of the institute of Mechanical Engineers, Series A 168 (1954) 371–394.
[54] R.D. Blevins, Formulas for Natural Frequency and Mode Shape, Krieger Publishing Company, Malabar, FL, USA, 1984.
[55] T. Hull, D.W. Clyne, An Introduction to Composite Materials, Cambridge Press, 1996.
[56] W.K. Liu, D. Qian, S. Gonella, S. Li, W. Chen, S. Chirputkar, International Journal for Numerical Methods in Engineering 83 (8–9) (2010) 1039–1080.
[57] Y. Chandra, R. Chowdhury, F. Scarpa, S. Adhikari, Thin Solid Films 519 (18) (2011) 6026–6032.
[58] K.I. Tserpes, P. Papanikos, Composites Part B: Engineering 36 (5) (2005) 468–477.
[59] T. Kaneko, Journal of Physics D: Applied Physics 8 (16) (1974) 1927–1936.
[60] D.W. Marquardt, Journal of the Society for Industrial and Applied Mathematics 11 (2) (1963) 431–441.
[61] J.S. Przemieniecki, Theory of Matrix Structural Analysis, McGraw-Hill, New York, 1968.
[62] K.J. Bathe, E.L. Wilson, Numerical Methods in Finite Element Analysis, Prentice-Hall, Englewood Cliffs, NJ, 1976.
[63] J.H. Wilkinson, The Algebraic Eigenvalue Problem, Oxford University Press, Oxford, UK, 1988.
[64] K. Behfar, R. Naghdabadi, Composites Science and Technology 65 (7–8) (2005) 1159–1164.
[65] F. Scarpa, S. Adhikari, A.J. Gil, C. Remillat, Nanotechnology 20 (12) (2010), 125702:1–9.
[66] K.N. Kudin, G.E. Scuseria, B.I. Yakobson, Phys. Rev. B 64 (23) (2001), 235406:1–10.
[67] O.A. Shenderova, V.V. Zhirnov, D.W. Brenner, Critical Reviews in Solid State and Materials Sciences 27 (3–4) (2002) 227–356.
[68] R.B. Karabalin, X.L. Feng, M.L. Roukes, Nano Letters 9 (9) (2009) 3116–3123.
[69] ANSYS Inc., Mechanical APDL Theory Manual, 2011.
[70] Kuang, Ken; Easler, Keith (Eds.), Fuel cell electronics packaging, Springer, (2007), pp. 254, ISBN-10/ASIN: 0387473238, ISBN-13/EAN: 9780387473239.